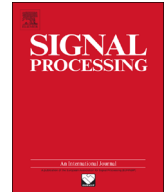




ELSEVIER

Contents lists available at ScienceDirect

Signal Processing

journal homepage: www.elsevier.com/locate/sigpro

On locality of Radon to Riesz transform

Laurent Desbat^{a,*}, Valérie Perrier^b^a University of Grenoble Alpes, TIMC-IMAG, CNRS UMR 5525, F-38000 Grenoble, France^b University of Grenoble Alpes, LJK, CNRS UMR 5224, F-38000 Grenoble, France

ARTICLE INFO

Article history:

Received 20 January 2015

Received in revised form

30 June 2015

Accepted 23 July 2015

Available online 14 August 2015

Keywords:

Riesz transform

Hilbert transform

Radon transform

Local reconstruction

ABSTRACT

In this paper we present a novel approach to locally compute the Riesz transform from the knowledge of the Radon transform. Previous implementations of the Riesz transform are based on the Fourier or the Radon transforms and their inversion formulae, and therefore needs for the knowledge of the function or its Radon data on the whole domain. More recent attempts on rectangular domains involves convolutions with the Poisson kernel and local derivatives. On the other hand, starting from the links between the Riesz and the Radon transforms, we address in this paper a new local Radon based Riesz formula in the general n -dimensional case, for even n . The advantage of this formula, *local in the Radon space*, is pointed out in the bidimensional case, where we provide a new local Radon based Riesz algorithm, and conduct numerical tests for the estimation of the Riesz transform on convex sets, *from truncated Radon data*. Finally we study the robustness to noise of the current approach.

© 2015 Elsevier B.V. All rights reserved.

1. Introduction

In image processing, the Riesz transform was introduced as a possible extension of the Hilbert Transform in general dimension. Contrarily to other extensions of the Hilbert transform, like the dimensional Hilbert transform or the total Hilbert transform that leads to quite high computational cost for truly bidimensional signals, the Riesz transform satisfies a steerable property with respect to rotation and thus is suitable for image analysis. The Riesz transform is also the way to construct the monogenic signal in several dimensions, which is the natural extension of the one dimensional analytic signal [9,7,8]. The monogenic signal, as well as the Riesz transform, have many applications in image processing or computer vision, like the demodulation of 2D fringe patterns [11], the extraction of local features in 2D signals [23,16,21,10,4],

the demodulation of holograms [17], or the analysis of color images [19].

The most easy way to implement the Riesz transform is to compute its Fourier representation by mean of 2D FFT. The disadvantage of such solution is first to require the whole knowledge of the 2D function, then to use a non-local filter. In image processing or for video applications, the Riesz transform is often applied on some bandpass filtered version of the image (by wavelets or pyramid decomposition), leading to approximate and faster implementations, even in the physical space [21,22,4]. Alternative approaches involve the Radon transform.

The Radon transform is widely used in medical imaging, for example in 2D tomography, modeling the X-ray attenuation through a patient in CT scanner. The conventional inversion of the Radon transform is the Filtered BackProjection (FBP) method, when all the data are available (global inversion). The filtering in the FBP formula is performed by the ramp filter, a commutative composition of Hilbert filtering and derivative. It is well known that the Hilbert Transform is a non-local operator. This leads to

* Corresponding author.

E-mail addresses: Laurent.Desbat@imag.fr (L. Desbat), Valerie.Perrier@imag.fr (V. Perrier).

reconstruction errors in the case of truncated projection data [12]. From 2002, a series of papers have proposed solutions to overcome this difficulty [14,13,5,2].

A first relation between the Riesz and the Radon transforms has been established in early works [7,9] (see also [18] for a recent FFT-based algorithm). Unfortunately, this relation between the Riesz and the Radon transforms involve non-local operators.

In this work we propose to overcome these drawbacks by deriving a new formula for the computation of the Riesz transform, *locally* from *local* Radon data, in even dimensional spaces. This local approach has many advantages: first, from the numeric point of view, it involves less computations than standard Radon based Riesz transform. Second, it provides an implementation of the Riesz transform or monogenic signal on convex regions, with an alternative method than these presented in [8] on rectangular domain. Finally, for medical applications, local approaches in the Radon domain allows for the use of small detectors [2].

The rest of the paper is organized as follows. Section 2 briefly re-introduces the transforms that will be used: the Hilbert transform, its natural multidimensional extension the Riesz transform, and the Radon transform. In Section 3 we recall the link between the Riesz and the Radon transforms, leading to the classical non-local Radon based Riesz approach. We then show how the Riesz transform can be computed locally from local Radon data in even dimension in Section 4, and we develop the bidimensional case. Finally, in Section 5.1, numerical experiments shows the interest of the method for the local estimation of the Riesz transform, from the knowledge of truncated Radon data. The robustness against noise, in the Radon domain as well as in the physical domain, is investigated.

2. Hilbert, Riesz and Radon transforms

2.1. 1-D Hilbert transform

Definition 1. Let $f \in \mathbb{L}^2(\mathbb{R})$ be a 1-D real valued function. The *Hilbert transform* of f , denoted by $\mathcal{H}f$, is defined as

$$\mathcal{H}f(t) \stackrel{\text{def}}{=} \left(\frac{1}{\pi} \text{vp} \left(\frac{1}{t} \right) * f \right)(t) = \lim_{\epsilon \rightarrow 0} \left(\frac{1}{\pi} \int_{|t-s| > \epsilon} \frac{f(s)}{t-s} ds \right) \text{ for a.e. } t \in \mathbb{R}.$$

The Hilbert transform can be computed easily in the Fourier domain¹: for a.e. $\xi \in \mathbb{R}$,

$$\widehat{\mathcal{H}f}(\xi) = -i \operatorname{sgn}(\xi) \widehat{f}(\xi).$$

Because of the discontinuity of sgn at origin, the Hilbert transform is a non-local operator. The Hilbert transform associates to any real function $f \in \mathbb{L}^2(\mathbb{R})$ a *complex analytic signal* $F = f + i\mathcal{H}f$, whose Fourier transform $\widehat{F} = (1 + \operatorname{sgn}(\xi))\widehat{f}$ vanishes on \mathbb{R}^- . The analytic signal is a way to uniquely

¹ The Fourier transform in \mathbb{R}^n is defined by $\widehat{f}(\vec{\xi}) = \int_{\mathbb{R}^n} f(\vec{x}) e^{-2i\pi \vec{x} \cdot \vec{\xi}} d\vec{x}$

associate to $f(t)$ local amplitude $A(t)$ and phase $\varphi(t)$ as, respectively, the modulus and argument of the analytic signal $F(t) = A(t)e^{i\varphi(t)}$.

2.2. n-D Riesz transform

The Riesz transform is the natural multidimensional extension of the Hilbert transform. We give below its definition in general dimension n .

Definition 2. Let $f \in \mathbb{L}^2(\mathbb{R}^n)$ be a real valued function. The Riesz transform of f , denoted by $\vec{R}f$, is the vector valued function:

$$\vec{R}f = \begin{pmatrix} R_1 f \\ \vdots \\ R_n f \end{pmatrix},$$

where for any $i = 1, \dots, n$, $R_i f$ is defined by

$$R_i f(\vec{x}) \stackrel{\text{def}}{=} \lim_{\epsilon \rightarrow 0^+} \left(\frac{1}{\pi \omega_{n-1}} \int_{\|\vec{x} - \vec{y}\| > \epsilon} \frac{(x_i - y_i)}{\|\vec{x} - \vec{y}\|^{n+1}} f(\vec{y}) d\vec{y} \right).$$

ω_{n-1} being the volume of the unit ball in \mathbb{R}^n . This rewrites in Fourier domain: for a.e. $\vec{\xi} \in \mathbb{R}^n$,

$$\widehat{\vec{R}f}(\vec{\xi}) = -i \frac{\vec{\xi}}{\|\vec{\xi}\|} \widehat{f}(\vec{\xi}). \quad (1)$$

The key properties of \vec{R} , crucial in image analysis, concern the invariance with respect to dilations, translations, and the steerability property (commutation with the rotations) [20,21].

2.3. Radon transform

Definition 3. Let \mathbb{S}^{n-1} denotes the unit sphere in \mathbb{R}^n ; the Radon Transform of $f \in \mathbb{L}^1(\mathbb{R}^n)$ is defined for all $s \in \mathbb{R}$ and $\vec{\theta} \in \mathbb{S}^{n-1}$, by

$$\mathcal{R}_{\vec{\theta}} f(s) \stackrel{\text{def}}{=} \mathcal{R}f(\vec{\theta}, s) \stackrel{\text{def}}{=} \int_{\vec{\theta}^\perp} f(s\vec{\theta} + \vec{y}) d\vec{y}. \quad (2)$$

where $\vec{\theta}^\perp = \{\vec{x} \in \mathbb{R}^n \mid \vec{x} \cdot \vec{\theta} = 0\}$ is the hyperplane orthogonal to the unit vector $\vec{\theta}$ (see Fig. 1 left, for the 2D-case).

The Radon transform is known to be invertible through the Fourier domain [12], using the projection-slice theorem which states that, for $\sigma \in \mathbb{R}$,

$$\widehat{\mathcal{R}_{\vec{\theta}} f}(\sigma) = \widehat{f}(\sigma \vec{\theta}) \quad (3)$$

This leads to the well-known filtered backprojection inversion formula:

$$f(\vec{x}) = \mathcal{R}^{-1}(\mathcal{R}f)(\vec{x}) \stackrel{\text{def}}{=} \int_{\mathbb{S}_{1/2}^{n-1}} \int_{\mathbb{R}} \widehat{\mathcal{R}_{\vec{\theta}} f}(\sigma) |\sigma|^{n-1} e^{2i\pi \sigma \vec{x} \cdot \vec{\theta}} d\sigma d\vec{\theta} \quad (4)$$

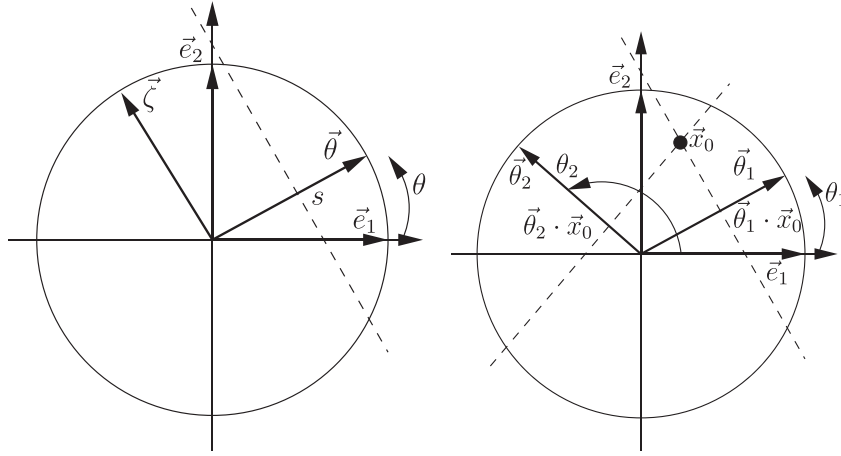


Fig. 1. 2D tomography. Left: parallel geometry parameters. The line of integration $s\vec{\theta} + \mathbb{R}\vec{\xi} = \{s\vec{\theta} + \vec{y}, \vec{y} \in \vec{\theta}^\perp\}$ is the dashed line. Right: two backprojection lines passing through \vec{x}_0 , $\vec{\theta}_1 \cdot \vec{x} = \vec{\theta}_1 \cdot \vec{x}_0$ and $\vec{\theta}_2 \cdot \vec{x} = \vec{\theta}_2 \cdot \vec{x}_0$. Local Radon data (θ, s) in the neighborhood of \vec{x}_0 correspond to lines $\vec{\theta} \cdot \vec{x} = s$ such that $|s - \vec{\theta} \cdot \vec{x}_0| < \varepsilon$ for some $\varepsilon > 0$.

where $\mathbb{S}_{1/2}^{n-1}$ is the half unit sphere in dimension n . Classically, Eq. (4) is computed through two steps [12]:

1. First a *filtering* of the Radon projections:

$$(\mathcal{R}_{\vec{\theta}} f)_{\mathbb{F}_R}(\vec{\theta}, s) = \int_{\mathbb{R}} \widehat{\mathcal{R}_{\vec{\theta}} f}(\sigma) |\sigma|^{n-1} e^{2i\pi\sigma s} d\sigma, \quad (5)$$

2. Then a *backprojection* of the filtered projections:

$$f(\vec{x}) = \mathcal{R}^\# \left((\mathcal{R}_{\vec{\theta}} f)_{\mathbb{F}_R} \right) (\vec{x})$$

where the backprojection operator is defined, for $g \in \mathbb{L}^1(\mathbb{S}^{n-1} \times \mathbb{R})$, by

$$\mathcal{R}^\#(g)(\vec{x}) = \int_{\mathbb{S}_{1/2}^{n-1}} g(\vec{\theta}, \vec{x} \cdot \vec{\theta}) d\vec{\theta}$$

Depending on the parity of dimension n , the filtering step (5) is a local operator or not. If n is odd, the filter $|\sigma|^{n-1}$ corresponds to a $(n-1)$ th derivative. Conversely if n is even, this filter is non local: in particular for $n=2$, it corresponds to the ramp filter $|\sigma| = \text{sgn}(\sigma)\sigma$, and (5) rewrites with the help of the Hilbert transform and the derivative of $\mathcal{R}_{\vec{\theta}} f$:

$$\begin{aligned} (\mathcal{R}_{\vec{\theta}} f)_{\mathbb{F}_R}(\vec{\theta}, s) &= \frac{1}{2\pi} \mathcal{H} \partial_s \mathcal{R}_{\vec{\theta}} f(s) \\ &= \lim_{\varepsilon \rightarrow 0^+} \frac{1}{2\pi^2} \int_{u \in \mathbb{R}; |s-u| > \varepsilon} \frac{\partial_s \mathcal{R}_{\vec{\theta}} f(u)}{s-u} du \end{aligned}$$

3. Non local Radon based Riesz transform

In order to recall the link between the Riesz and the Radon transforms, we proceed directly by considering the

inverse Fourier formula of the Riesz transform:

$$\begin{aligned} \vec{R}f(\vec{x}) &= \int_{\mathbb{R}^n} \widehat{R}f(\vec{\xi}) e^{2i\pi \vec{x} \cdot \vec{\xi}} d\vec{\xi} \\ &= \int_{\mathbb{S}_{1/2}^{n-1}} \int_{\mathbb{R}} \widehat{R}f(\sigma \vec{\theta}) e^{2i\pi \sigma \vec{x} \cdot \vec{\theta}} |\sigma|^{n-1} d\sigma d\vec{\theta} \end{aligned}$$

making the spherical change of variable $\vec{\xi} = \sigma \vec{\theta}$ with $\sigma \in \mathbb{R}$ and $\vec{\theta} \in \mathbb{S}_{1/2}^{n-1}$. From (1) and the projection slice theorem (3), we have

$$\widehat{R}f(\sigma \vec{\theta}) = -i \frac{\sigma}{|\sigma|} \widehat{f}(\sigma \vec{\theta}) = -i \text{sgn}(\sigma) \widehat{\mathcal{R}_{\vec{\theta}} f}(\sigma \vec{\theta}) \quad (6)$$

Then,

$$\vec{R}f(\vec{x}) = \int_{\mathbb{S}_{1/2}^{n-1}} \int_{\mathbb{R}} -i \text{sgn}(\sigma) \widehat{\mathcal{R}_{\vec{\theta}} f}(\sigma \vec{\theta}) e^{2i\pi \sigma \vec{x} \cdot \vec{\theta}} |\sigma|^{n-1} d\sigma d\vec{\theta}. \quad (7)$$

The formula (7) has been already established in previous works [7,16,18] for the construction of the 2D Riesz transform. But the developments often proposed for its practical application were based on the following remark: (7) rewrites in the bidimensional case:

$$\begin{aligned} \vec{R}f(\vec{x}) &= \int_0^\pi \int_{\mathbb{R}} \left(\widehat{\mathcal{R}_{\vec{\theta}} f}(\sigma) (-i) \text{sgn}(\sigma) \right) |\sigma| e^{2i\pi \sigma \vec{x} \cdot \vec{\theta}} d\sigma d\theta \\ &= \int_0^\pi \left(\int_{\mathbb{R}} \mathcal{H} \widehat{\mathcal{R}_{\vec{\theta}} f}(\sigma) |\sigma| e^{2i\pi \sigma \vec{x} \cdot \vec{\theta}} d\sigma \right) \vec{\theta} d\theta \end{aligned} \quad (8)$$

with the Hilbert transform \mathcal{H} . Using expression (4) of the inverse Radon transform \mathcal{R}^{-1} , (8) finally writes

$$\vec{R}f(\vec{x}) = \mathcal{R}^{-1} \left((\mathcal{H} \mathcal{R}_{\vec{\theta}} f) \vec{\theta} \right) (\vec{x}) \quad (9)$$

The Riesz transform of f is then obtained from an Hilbert filtering followed by the Radon inversion operator. In the following, we will call this method $i\text{RadonH}$. Fig. 2 synthesizes the links between these transforms, and the

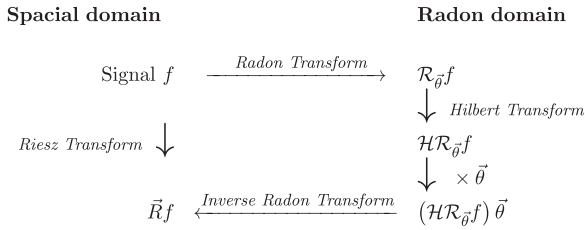


Fig. 2. Relations between Radon, Riesz, and Hilbert transform [9,7].

following algorithm summarizes the different steps of $i\text{RadonH}$ necessary to reconstruct the Riesz transform from the Radon data (extracted from [7]):

Algorithm 1. $i\text{RadonH}$: Radon based Riesz classical algorithm [9].

1. Compute $\mathcal{H}(\mathcal{R}_{\vec{\theta}}(f))$ the Hilbert transform of $\mathcal{R}_{\vec{\theta}}f$ (according to the real variable s).
2. Multiply $\mathcal{H}\mathcal{R}_{\vec{\theta}}f$ by $\cos \theta$ and $\sin \theta$.
3. Compute the inverse Radon transforms of $\mathcal{H}(\mathcal{R}_{\vec{\theta}}(f)) \cos \theta$ and of $\mathcal{H}(\mathcal{R}_{\vec{\theta}}(f)) \sin \theta$.

The main advantage of Eq. (9) is to allow for the use of simple operators such as the inverse Radon operator and the Hilbert operator (if available). But, its main drawback is to contain non-local operators: \mathcal{H} is non-local on $\mathcal{R}_{\vec{\theta}}f$ and \mathcal{R}^{-1} is non-local in even dimension on its argument. This implies that the complete knowledge (or computation) of $\mathcal{R}f$ is needed for computing $\vec{R}f$ at a given point \vec{x} . The next section will introduce a new reconstruction formula, involving only local operators in even dimension.

4. A new local Radon based Riesz transform in even dimension

4.1. New approach in nD , local for n even

Eq. (7) is now splitted into two integral operations: the Riesz transform can be computed through the two following steps:

1. First a filtering of the Radon projections

$$(\mathcal{R}f)_{F_{\vec{R}}}(\vec{\theta}, s) = \int_{\mathbb{R}} \widehat{\mathcal{R}_{\vec{\theta}}f}(\sigma) e^{2i\pi s \sigma} (-i) \text{sgn}(\sigma) |\sigma|^{n-1} d\sigma \quad (10)$$

2. Followed by a vectorial weighted (by the components of $\vec{\theta}$) backprojection

$$\vec{R}f(\vec{x}) = \int_{\mathbb{S}_{1/2}^{n-1}} (\mathcal{R}f)_{F_{\vec{R}}}(\vec{\theta}, \vec{x} \cdot \vec{\theta}) \vec{\theta} d\vec{\theta} \quad (11)$$

A new, depending on the parity of integer n , the filtering is a local operator or not. We remark in Eq. (10) that if n is even then $\text{sgn}(\sigma) |\sigma|^{n-1} = \sigma^{n-1}$ whereas if n is odd then $\text{sgn}(\sigma) |\sigma|^{n-1} = \text{sgn}(\sigma) \sigma^{n-1}$. Thus if n is even the

filter is a $(n-1)$ th derivative according to s . On the contrary, if n is odd, the filter is the composition of the Hilbert (non-local) filtering with the $n-1$ time derivative. Finally step 1 is a local filter only for even n .

4.2. New local formula in 2D

In the bidimensional case, the Riesz transform of a given function f can be simply computed from its Radon data, by the following reconstruction formula.

Proposition 1. Let f be a sufficiently regular bidimensional function. We have

$$\vec{R}f(\vec{x}) = -\frac{1}{2\pi} \int_0^\pi \frac{\partial \mathcal{R}f}{\partial s}(\vec{\theta}, \vec{x} \cdot \vec{\theta}) \vec{\theta} d\theta \quad (12)$$

where $\vec{R}f$ and $\mathcal{R}f$ denote respectively the Riesz and Radon transforms of f .

Proof. We consider now Eqs. (10), (11). Eq. (10) becomes

$$\begin{aligned} (\mathcal{R}f)_{F_{\vec{R}}}(\vec{\theta}, s) &= \int_{\mathbb{R}} \widehat{\mathcal{R}_{\vec{\theta}}f}(\sigma) (-i \text{sgn}(\sigma)) |\sigma| e^{2i\pi s \sigma} d\sigma \\ &= \int_{\mathbb{R}} \widehat{\mathcal{R}_{\vec{\theta}}f}(\sigma) (-i) \text{sgn}(\sigma) \text{sgn}(\sigma) \sigma e^{2i\pi s \sigma} d\sigma \\ &= \int_{\mathbb{R}} \widehat{\mathcal{R}_{\vec{\theta}}f}(\sigma) \frac{-i}{2i\pi} (2i\pi \sigma) e^{2i\pi s \sigma} d\sigma \\ &= -\frac{1}{2\pi} \int_{\mathbb{R}} \widehat{\mathcal{R}_{\vec{\theta}}f}(\sigma) (2i\pi \sigma) e^{2i\pi s \sigma} d\sigma \\ &= -\frac{1}{2\pi} d \frac{\mathcal{R}_{\vec{\theta}}f}{ds}(s) = -\frac{1}{2\pi} \frac{\partial \mathcal{R}f}{\partial s}(\vec{\theta}, s) \square \end{aligned} \quad (13)$$

In (12), the Riesz transform of f is computed from its Radon data with just the derivative of the Radon projections (local operation) followed by a weighted back projection (local in the Radon framework). This new method will be called BPD (BackProjection of the Derivative) in the following. Its principle is sketched in Fig. 3, and Algorithm 2 below summarizes the different steps of BPD needed to compute the Riesz transform of f from its Radon projections.

Algorithm 2. BPD: local Radon based Riesz algorithm.

1. Compute $(\partial/\partial s)\mathcal{R}(f)$ the partial derivative of $\mathcal{R}f$.
2. Multiply $(\partial/\partial s)\mathcal{R}(f)$ by $-1/2\pi$, then respectively by $\cos \theta$ and by $\sin \theta$.
3. Compute the backprojections respectively of $(-1/2\pi)(\partial/\partial s)\mathcal{R}(f) \cos \theta$ and of $(-1/2\pi)(\partial/\partial s)\mathcal{R}(f) \sin \theta$.

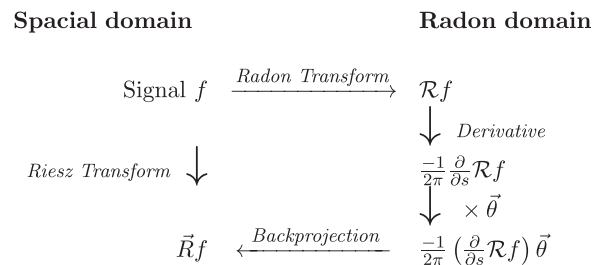


Fig. 3. Local bidimensional Radon to Riesz links.

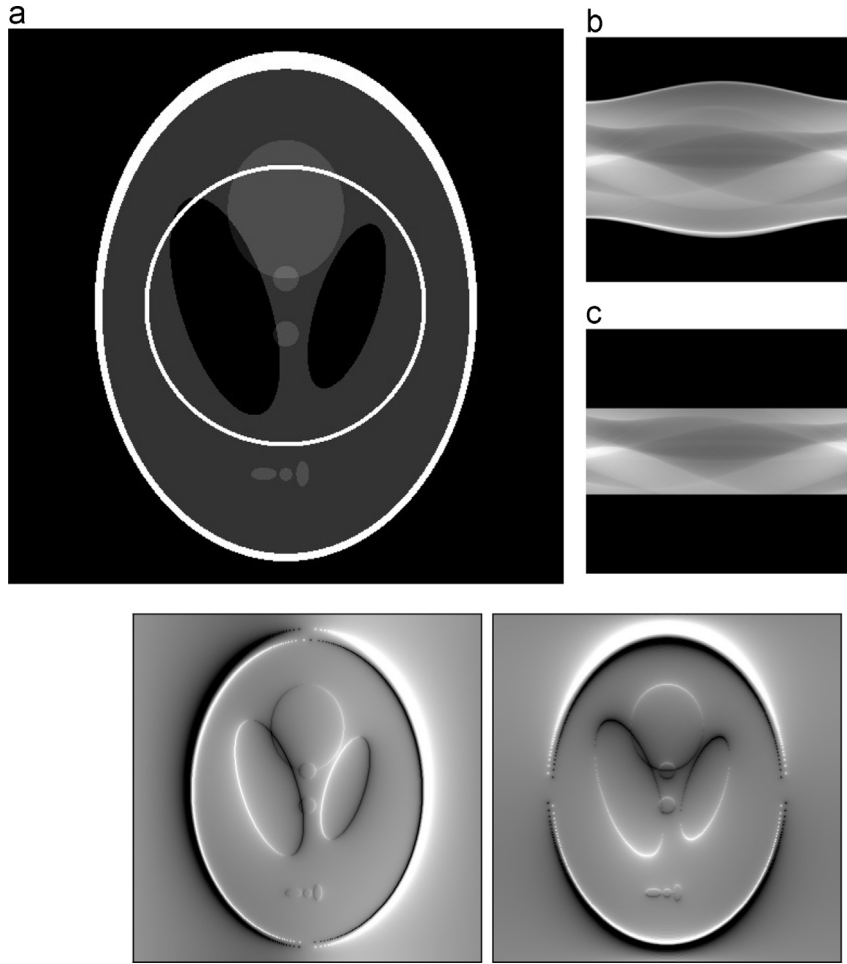


Fig. 4. (a) Shepp and Logan (512×512) phantom with the considered ROI (materialized by a white circle) and (b) corresponding sinogram (discretized Radon data: equiangular and equispaced 806×512 samples on $[0, \pi) \times$ the diagonal of the image). (c) Truncated Radon projections: only the lines passing through the ROI are measured. Last line: Riesz transform computed using FFT (FFTRiesz from Eq. (1)); first component (left) and second component (right).

Note that in [Algorithm 2](#) step 1 is *local*, and step 3 is a *local* operation in the Radon sense, whereas in [Algorithm 1](#) neither step 1 nor step 3 are.

Remark. In (12), the computation of $\vec{R}f(\vec{x}_0)$ at a given point \vec{x}_0 only requires the knowledge of the line integrals (Radon data) $\mathcal{R}f(\vec{\theta}, s)$ passing in a neighborhood of \vec{x}_0 , i.e. the lines $(\vec{\theta}, s)$ such that $|\vec{x} \cdot \vec{\theta} - s| < \varepsilon$ for some small positive ε . The estimation of the Riesz transform $\vec{R}f$ on some disk $\mathcal{D}(\vec{x}, r)$ centered at \vec{x} with radius r , is then exactly recovered from Radon data $(\vec{\theta}, s)$ such that $|\vec{x} \cdot \vec{\theta} - s| < r + \varepsilon$, i.e. a sinusoidal strip in the Radon variable space for some $\varepsilon > 0$. On the contrary, computing $\vec{R}f(\vec{x})$ from formula (9) needs $\mathcal{R}f(\vec{\theta}, s)$ for all $(\vec{\theta}, s)$. This remark can be easily generalized to computing the Riesz transform on convex sets from Radon data on strips of variable width.

5. Numerical experiments

In this section we present Riesz transform computations, from the global and local points of view, where we compare the results provided by our reconstruction formula (BPD [Algorithm 2](#)), with those of the formula of the literature (iRadonH [Algorithm 1](#)). We also compare BPD with FFTRiesz, the method computing the Riesz transform directly using the Fast Fourier Transform (FFT) from the zero padded images (Eq. (1)), and with PyrRiesz, a pyramidal Riesz transform derived from the supplementary material² from [22].

Finally we investigate the robustness to noise, in the Radon domain as well as in the physical domain, of the local-Radon approach, with respect to comparable methods. We used standard images from medical imaging (Shepp and Logan phantom) or image processing (Lenna). The numerical experiments have been developed with

² see <http://people.csail.mit.edu/nwadhwa/riesz-pyramid/>

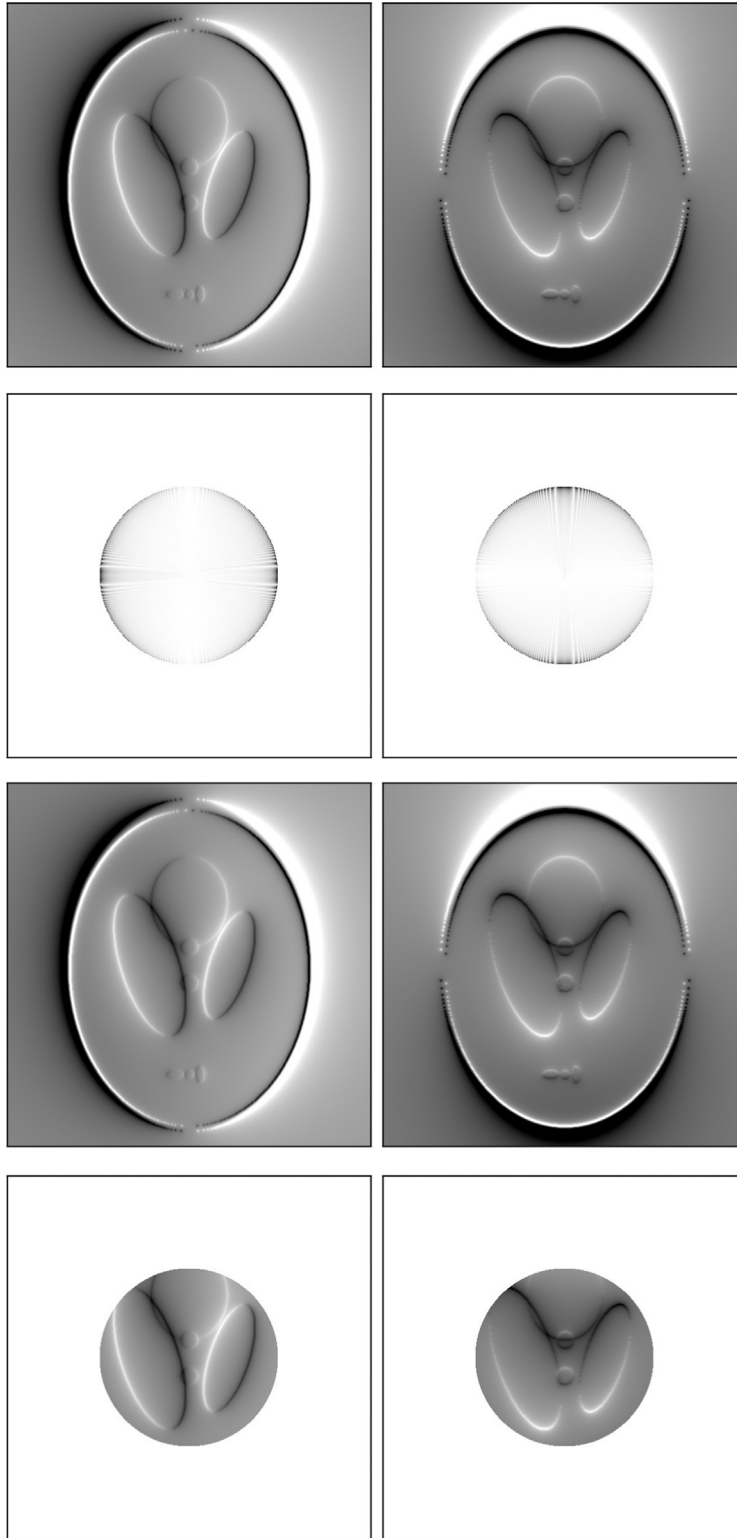


Fig. 5. Shepp and Logan phantom Riesz transforms: First line computed with the *non local* $iRadonH$ formula (9) from the full Radon data. Second line: Error in the ROI between the $iRadonH$ results from the truncated (ROI) Radon data, and $iRadonH$ results from full Radon data (first line). Third line, computed with the *local* BPD formula (12) from the full Radon data, fourth line from the truncated (ROI) Radon data. In each case, first component (left) and second component (right).

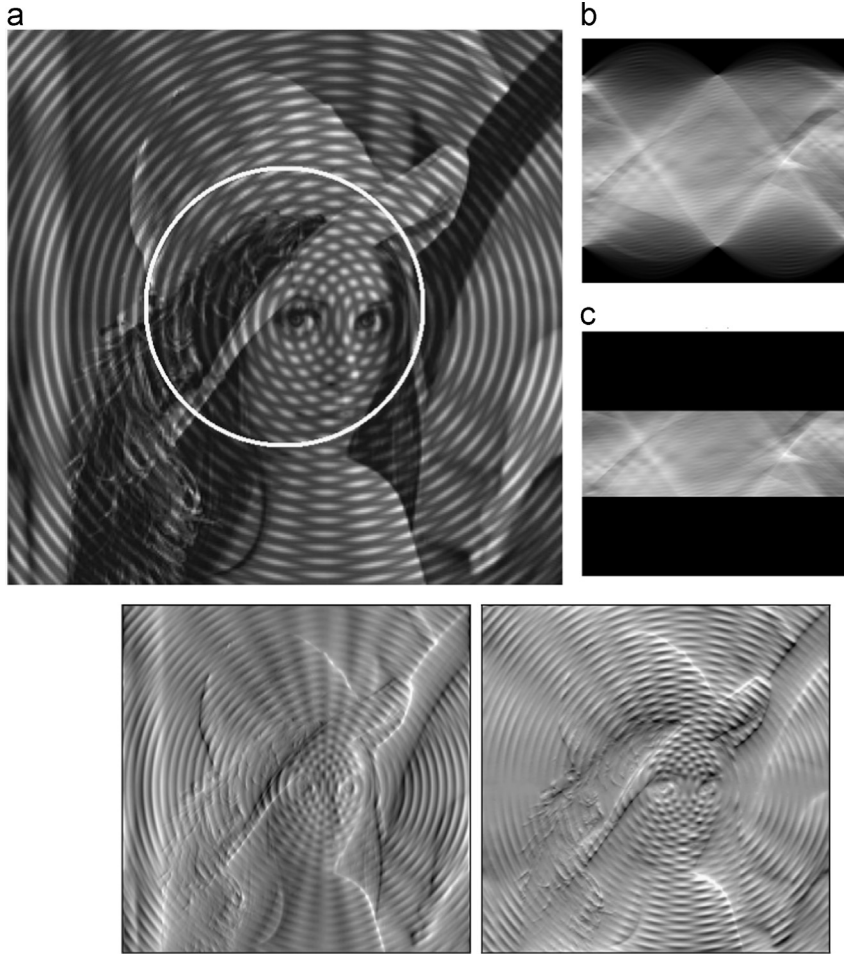


Fig. 6. (a) Psychedelic Lenna image (of size 512×512) with the considered ROI (materialized by a white circle) and (b) corresponding sinogram (discretized Radon data: equiangular and equispaced 806×512 samples on $[0, \pi] \times$ the diagonal of the image). (c) Truncated Radon projections: only the lines passing through the ROI are measured. Last line, psychedelic Lenna Riesz transform computed using FFT (FFTRiesz Eq. (1)): first component (left) and second component (right).

MATLAB providing standard Hilbert, Radon and inverse Radon transforms.

5.1. Modified Shepp and Logan

Our first numerical test 512×512 image f is the well known modified Shepp and Logan phantom, available in MATLAB and shown in Fig. 4 (that we simply call “Shepp and Logan phantom” in the following). The full 806×512 sinogram on $[0, \pi[$ computed with the MATLAB `radon` command is shown in (b). We also provide in Fig. 4 the two components of its Riesz transform, directly computed using the Fast Fourier Transform (FFT) (Eq. (1)), denoted `FFTRiesz`.

We now consider a ROI (Region Of Interest) of the image f . We suppose that the only Radon data available $\mathcal{R}_{\vec{\theta}} f(s)$ are the integral of f on lines intersecting the ROI, i.e. lines $(\vec{\theta}, s)$ for which there exists \vec{x} in the ROI such that $\vec{\theta} \cdot \vec{x} = s$. If the ROI does not fully contains the support of f , Radon data truncations occur. In Fig. 4 we consider for the ROI a centered disk of radius of 128 pixels (white circle

in (a)). This leads to truncated Radon projections (Fig. 4 (c)).

We first compute the Riesz transform of f from its Radon data using the classical method `iRadonH` (9). The formula is applied to both the full Radon data (Fig. 4(b)) and the truncated Radon data (Fig. 4(c)). The obtained results are shown in Fig. 5 (top).

The second line of Fig. 5 highlights the spacial error provided by `iRadonH` formula (9), between the Riesz transform of f computed from the full Radon data (Fig. 4(b)) and the Riesz transform computed from the truncated Radon data (Fig. 4(c)). Precisely, the maximum of the relative error absolute value in the ROI corresponds to 49.14% for the first Riesz component and 68.49% for the second Riesz component, which is large. We then compute the Riesz transform of f from its Radon data using the local method `BPD` (12). As previously, the formula is applied to both the full Radon data (from Fig. 4 (b)) and the truncated (ROI) Radon data (from Fig. 4(c)). The obtained results are shown in Fig. 5 (bottom).

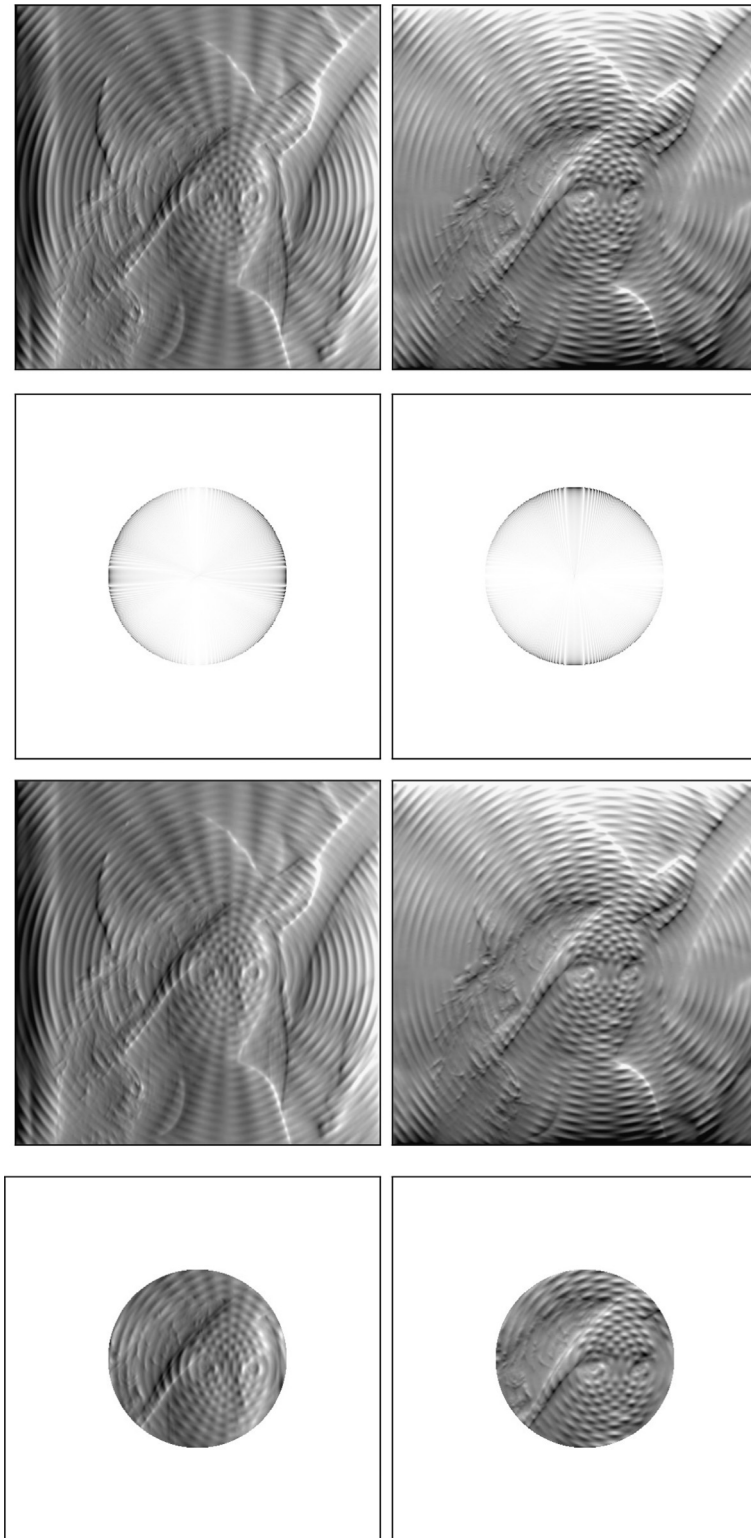


Fig. 7. Psychedelic Lenna Riesz transforms: First line computed with the *non local* $i\text{RadonH}$ formula (9) from the full Radon data. Second line, difference between the $i\text{RadonH}$ method applied to full Radon data (first line) and applied to truncated (ROI) Radon data. Third line computed with the *local* BPD formula (12) from the full Radon data, fourth line from the truncated (ROI) Radon data. In each case, first component (left) and second component (right).

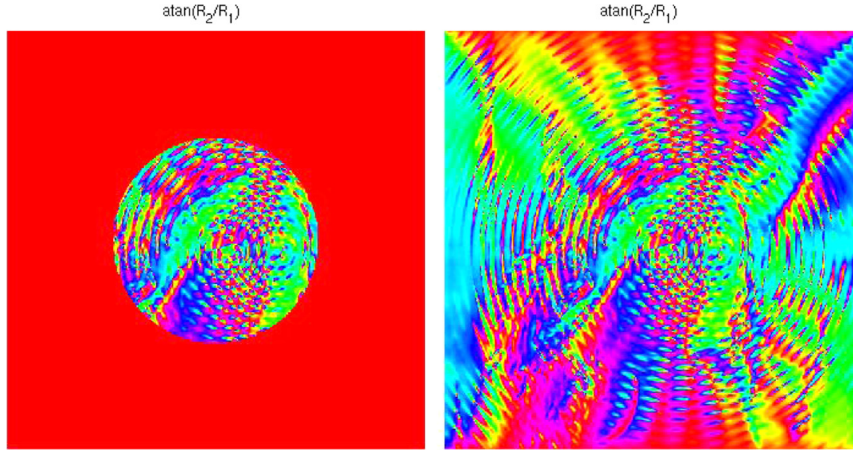


Fig. 8. $\arctan(R_2/R_1)$ computed with the BPD formula (Eq. (12)) from truncated projections (left) and from full projections (right).

Contrary to $iRadonH$ which yields an error in the ROI shown in second line, the formula BPD (Eq. (12)) yields no error in the ROI.

5.2. Psychedelic Lenna

We present now numerical experiments on an image processing 512×512 test image (more precisely the so-called Psychedelic Lenna [21]), see Fig. 6. The full 806×512 sinogram on $[0, \pi]$ is shown in (b). A ROI, centered disk of radius of 128 pixels, is considered (white circle in (a)). This leads to truncated Radon projections (c).

Fig. 6 (bottom) shows the two components of the Psychedelic Lenna images Riesz transform directly computed using the Fast Fourier Transform (with $FFTRiesz$, Eq. (1)).

We first compute in Fig. 7 (top) the Riesz transform of the image from its Radon data using the classical method $iRadonH$ (9). The formula is applied to both the full Radon data (from Fig. 6(b)) and the truncated (ROI) Radon data (from Fig. 6(c)). Artifacts near the boundary of the ROI can be seen in the $iRadonH$ applied to truncated Radon data. The second row of Fig. 7 highlights the spacial error provided by $iRadonH$ formula (9), between the Riesz transform of the images computed from the full Radon data and the Riesz transform computed from the truncated Radon data. Precisely, the maximum of the relative error absolute value in the ROI corresponds to 75.91% for the first Riesz component and 75.45% for the second Riesz component of psychedelic Lenna image.

We then compute the Riesz transform of the image from its Radon data using the local method BPD (12). As previously, the formula is applied to both the full Radon data (from Fig. 6(b)) and the truncated (ROI) Radon data (from Fig. 6(c)). The obtained results are shown in Fig. 7 (bottom). Contrary to $iRadonH$, BPD yields exactly the same numerical results in the ROI from full or truncated Radon data.

The Riesz Transform (as well as the monogenic signal) is often used to define and compute orientations of multi-dimensional signals (see for example [21]). In Fig. 8 we compute pointwise the orientation $\vec{\theta}(\vec{x})$ of $\vec{R}(\vec{x})$, i.e. $\vec{\theta}(\vec{x}) = (\cos \theta(\vec{x}), \sin \theta(\vec{x})) = (R_1 f(\vec{x}), R_2 f(\vec{x})) / \|\vec{R}(\vec{x})\|$, where the Riesz transform is computed with the

Table 1

Error of the second reconstructed Riesz component of the 1024×1024 image discretization I of f_{\cos} on $[0, 1) \times [0, 1)$ computed with the method M being either $FFTRieszBPD$ or $PyrRiesz$ compared to f_{\sin} excluding strips of 100 pixel width on the boundary of the 1024×1024 image.

M	$FFTRiesz$	BPD	$PyrRiesz$
$\ (R_2 I)_M - f_{\sin}\ _{\infty}$	0.01	0.07	0.20
$\ (R_2 I)_M - f_{\sin}\ _2$	0.002	0.04	0.13

BPD approach from local Radon data. Note that the improvement proposed in [21] section I.E, using a structure tensor formalism with a convolution by a smooth local kernel $v(\vec{x})$, in order to build a robust estimate, can also be applied here. Thus the locality advantages of BPD can be fully exploited to locally compute orientations $\theta(\vec{x})$ in a reduced ROI, with no difference compare to the complete projections (in case of truncated projections the size of the ROI would be reduced according to the size of the support of the convolution filter $v(\vec{x})$).

5.3. Comparison of BPD with $FFTRiesz$ and $PyrRiesz$

In this section we compare BPD with two other Riesz algorithms, $FFTRiesz$ and $PyrRiesz$. $FFTRiesz$ is the Riesz transform computed with the FFT applied to a zero padded image, see (1). $PyrRiesz$ is a pyramidal Riesz transform that can be derived from the supplementary material³ of [22]. As proposed in [22], we have used the three tap finite difference filters $[0.5, 0, -0.5]$ and its transpose $[0.5, 0, -0.5]^T$ to compute both highpass Riesz components from the highpass pyramid components. Both lowpass residual Riesz components are computed here with $FFTRiesz$ applied to the lowpass residual pyramid component.

We first consider I the $n \times n$ image discretization of $f_{\cos}(\vec{x}) = \cos(2k\pi x_2/n)$ on $[0, 1) \times [0, 1)$ with $k=10$ and $n=1024$. The Riesz transform of f_{\cos} is $\vec{R}f_{\cos} = (0, f_{\sin})$

³ see <http://people.csail.mit.edu/nwadhwa/riesz-pyramid/>

with $f_{\sin}(\vec{x}) = \sin(2k\pi x_2/n)$. Thus except on the boundary of the $n \times n$ image, we assume that the second component of the Riesz transform of the $n \times n$ image I is close to the $n \times n$ image discretization of $f_{\sin}(\vec{x})$. In Table 1 we

compare $|(R_2 I)_M - f_{\sin}|$ for the three methods $M \in \{\text{FFTRiesz}, \text{BPD}, \text{PyrRiesz}\}$. The norm is computed on the image excluding a strip of 100 pixel width on the boundary of the image, i.e. on $[101:924] \times [101:924]$ pixels

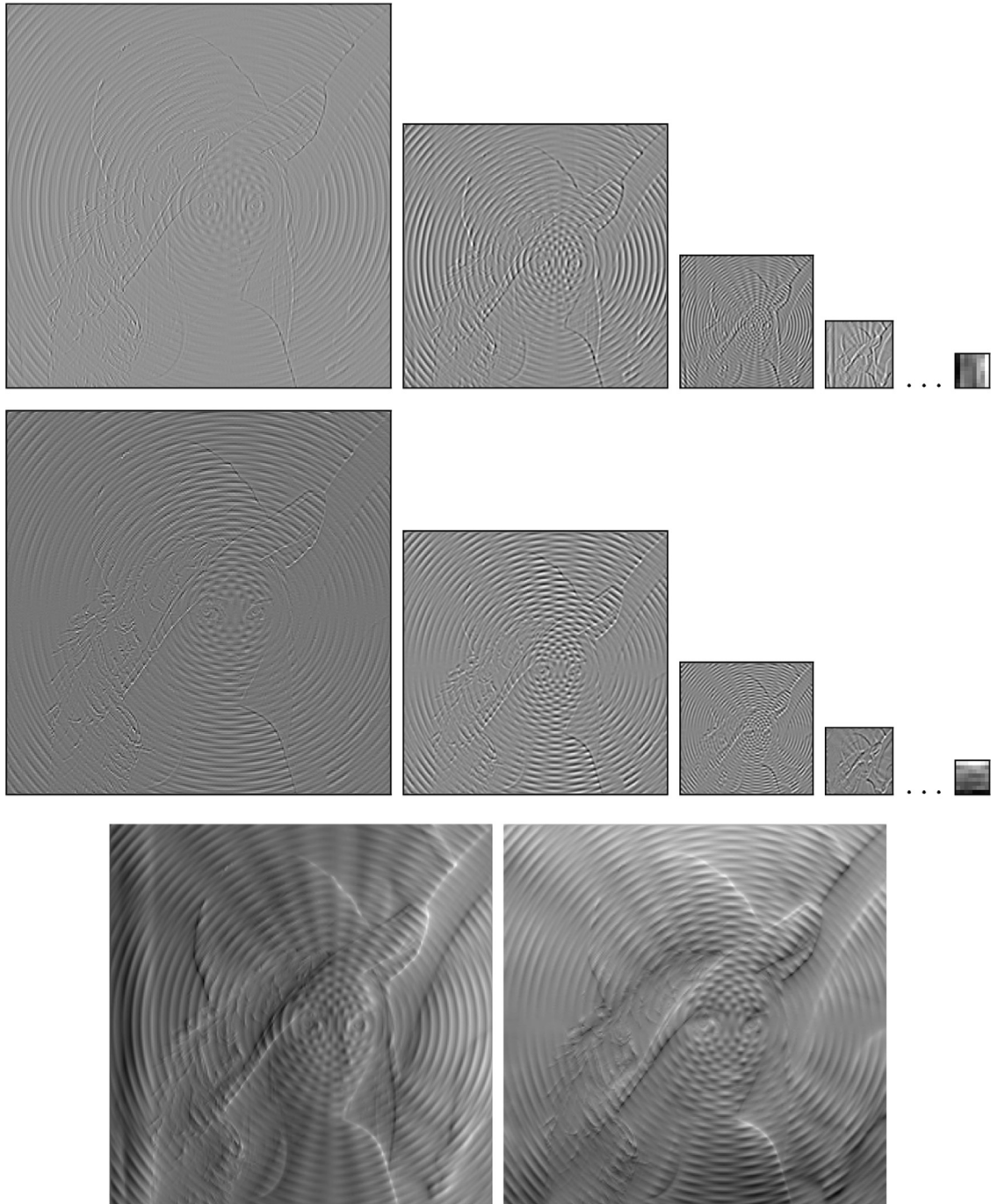


Fig. 9. The pyramidal Riesz transform PyrRiesz applied to Psychedelic Lenna. First (resp. second) line: highpass Riesz first (resp. second) components derived from the three tap finite difference filters applied to the highpass pyramid components (for both Riesz components we show the four first pyramidal components); for both lines the last image is the lowpass residual Riesz first (resp. second) component obtained with FFTRiesz applied the lowpass residual pyramid component. Note that for a better global visualisation, for both lines, the first and last images have been rescaled. Third line, first (left) and second (right) Riesz components reconstructed from the two previous lines PyrRiesz (to be compared to Fig. 6 last line).

Table 2Relative error of the reconstructed Riesz components from BPD and PyrRiesz compared to FFTRiesz excluding strips of width S_{oW} pixels.

	$\frac{\ (R_{jf})_{\text{PyrRiesz},S_{oW}} - (R_{jf})_{\text{FFTRiesz},S_{oW}}\ _{\infty}}{\ (R_{jf})_{\text{BPD},S_{oW}} - (R_{jf})_{\text{FFTRiesz},S_{oW}}\ _{\infty}}$		$\frac{\ (R_{jf})_{\text{PyrRiesz},S_{oW}} - (R_{jf})_{\text{FFTRiesz},S_{oW}}\ _2}{\ (R_{jf})_{\text{BPD},S_{oW}} - (R_{jf})_{\text{FFTRiesz},S_{oW}}\ _2}$	
j	1	2	1	2
$S_{oW}=2$	1.6	2.1	2.2	1.9
$S_{oW}=10$	0.8	0.9	1.9	1.6
$S_{oW}=20$	0.8	0.8	1.9	1.6

Table 3Stability of BPD or iRadonH methods in case of noisy Radon projections. The $\|\cdot\|$ are computed in the ROI for both BPD and iRadonH. iRadonH is computed from non-truncated projections. When iRadonH is computed from truncated projections, the errors are dominated by the error due to truncation, see Table 4.

M	$100 \frac{\ (R_{jf})_{M,\epsilon_L} - (R_{jf})_M\ _{\infty}}{\ (R_{jf})_M\ _{\infty}}$				$100 \frac{\ (R_{jf})_{M,\epsilon_L} - (R_{jf})_M\ _2}{\ (R_{jf})_M\ _2}$			
	BPD		iRadonH		BPD		iRadonH	
j	1	2	1	2	1	2	1	2
$L=0.1$	0.8	1.0	1.6	1.6	0.7	0.8	1.4	1.7
$L=0.5$	4.0	5.6	9.1	9.3	3.6	4.3	7.3	8.4
$L=1$	8.6	9.9	16.1	17.1	7.1	8.4	14.8	16.6
$L=3$	24.4	29.8	50.9	49.4	21.9	24.8	44.6	49.4

(instead of the $[1:1024] \times [1:1024]$ in order to exclude boundary errors). We see that FFTRiesz and f_{sin} are close (apart on the image boundary) and that BPD yields slightly closer results than PyrRiesz does.

Accordingly in the following, FFTRiesz will be supposed to be our gold standard reference method. We now show in Fig. 9 the Riesz Pyramid of Psychedelic Lenna computed with PyrRiesz.

In Table 2 we show the ratio of the relative errors to FFTRiesz of the reconstructed Riesz components $j \in \{1, 2\}$ with BPD and with PyrRiesz:

$$\frac{\|(R_{jf})_{\text{PyrRiesz},S_{oW}} - (R_{jf})_{\text{FFTRiesz},S_{oW}}\|}{\|(R_{jf})_{\text{BPD},S_{oW}} - (R_{jf})_{\text{FFTRiesz},S_{oW}}\|}$$

Because largest errors occur on the boundary of the image, we compute the relative error excluding a strip of width S_{oW} pixels on the boundary of the image. We see that the ratio is close to 1 indicating the same level of error of both methods compared to FFTRiesz. We note that the $\|\cdot\|_2$ error of BPD seems always to be smaller but the PyrRiesz error in $\|\cdot\|_{\infty}$ is smaller compare to BPD (except on the boundary of the image).

Using the pyramidal transform of [22] and three tap finite difference filters to derive a pyramidal Riesz transform PyrRiesz yields a much faster method compare to BPD. In [22], the linear computational cost of PyrRiesz is estimated at 99 multiplies per pixels, i.e. $99n^2$ where n^2 is the pixel number. The cost of our BPD is $O(n^3)$ (cost order for a (Radon) projection and for a backprojection). Fast Radon projection and backprojection (see [1,15]) have a theoretical computational cost of $O(n^2 \log_2(n))$ and a practical effective cost larger than the FFT cost. Thus PyrRiesz, designed to be faster than FFTRiesz, is the fastest method here to compute the Riesz transform of an image.

However, BPD is designed to compute the Riesz transform from its Radon projections. In this context BPD is more efficient than iRadonH and PyrRiesz is not appropriate.

5.4. Sensitivity to noise

We study the robustness against noise of the methods, first in the case of additive noise on the Radon projection data $\mathcal{R}f$, then in the case of additive noise on the original image f .

First, we consider the modified Shepp and Logan phantom and assume that the data are the Radon projections $\mathcal{R}_{\vec{\theta}}f(s)$ (usually extracted through gain, offset and logarithmic corrections from radiographic data). A common approximation of the noise on such data in the context of medical imaging is a centered Gaussian additive noise proportional to the value $\mathcal{R}_{\vec{\theta}}f(s)$ [6,3]. In the following we add to $\mathcal{R}_{\vec{\theta}}f(s)$ the noise value $\epsilon_L(\vec{\theta}, s) = \mathcal{R}_{\vec{\theta}}f(s)(L/100)\epsilon_{\vec{\theta},s}$, where L is a noise level (in %) and $\epsilon_{\vec{\theta},s} \sim \mathcal{N}(0, 1)$ ($\mathcal{N}(0, 1)$ is the standard normal distribution). L larger than 1 is considered as high noise. Remark that here, the Fourier method FFTRiesz is not directly applicable to compute the Riesz Transform, because only Radon data are supposed to be available. We thus consider only the stability against noise of the Radon to Riesz methods using BPD or iRadonH. We denote by $(R_{jf})_{\text{BPD},\epsilon_L}$, resp. $(R_{jf})_{\text{iRadonH},\epsilon_L}$, the R_{jf} component ($j \in \{1, 2\}$) obtained from noisy Radon projections with the BPD method, resp. iRadonH, and by $(R_{jf})_{\text{BPD}}$, resp. $(R_{jf})_{\text{iRadonH}}$, the corresponding R_{jf} component obtained from data without noise. In Table 3 we study the error $\frac{\|(R_{jf})_{M,\epsilon_L} - (R_{jf})_M\|}{\|(R_{jf})_M\|}$ for both methods $M \in \{\text{BPD}, \text{iRadonH}\}$ (in %). We see that the errors due to noise remain relatively small for low noise level (0.1, 0.5 and even 1). For larger noise level, the derivative would

Table 4

Stability of $iRadonH$: the $\|\cdot\|$ are computed in the ROI but now $iRadonH$ is computed from truncated projections. The errors due to truncation are dominant.

	$100 \frac{\ (R_j f)_{iRadonH, \epsilon_L} - (R_j f)_{iRadonH}\ _{\infty}}{\ (R_j f)_{iRadonH}\ _{\infty}}$	$100 \frac{\ (R_j f)_{iRadonH, \epsilon_L} - (R_j f)_{iRadonH}\ _2}{\ (R_j f)_{iRadonH}\ _2}$
j	1	2
$L=0.1$	49.3	68.9
$L=0.5$	49.9	72.2
$L=1$	49.1	72.9
$L=3$	70.8	94.1
	1	2
	26.8	35.0
	27.7	36.2
	30.7	39.1
	53.2	62.6

Table 5

Stability of BPD, $iRadonH$ and $FFTRiesz$ methods in case of Psychedelic Lenna corrupted by additive Gaussian noise of level L .

M	$100 \frac{\ (R_j f)_{M, \epsilon_L} - (R_j f)_M\ _{\infty}}{\ (R_j f)_M\ _{\infty}}$						$100 \frac{\ (R_j f)_{M, \epsilon_L} - (R_j f)_M\ _2}{\ (R_j f)_M\ _2}$					
	FFTRiesz		BPD		$iRadonH$		FFTRiesz		BPD		$iRadonH$	
j	1	2	1	2	1	2	1	2	1	2	1	2
$L=1$	4.4	6.4	2.0	2.2	2.4	3.3	5.0	6.4	1.7	2.2	2.5	3.1
$L=3$	16.7	20.8	5.7	6.7	8.3	9.4	15.0	19.1	5.4	6.8	7.5	9.4

need a more sophisticated scheme than just a local finite difference scheme, adding some filtering (such as Sobel, Gaussian, ...). Table 4 shows big errors, even for low noise levels: indeed the error due to truncation when computing $iRadonH$ from truncated projections is much larger than the error due to noise.

Then we considered the Psychedelic Lenna image, on which we directly added a Gaussian noise, $f(x, y) + \epsilon_L(x, y)$ where $\epsilon_L(x, y) = (L/100) \|f\|_{\infty} \epsilon_{x,y}$, with $\epsilon_{x,y} \sim \mathcal{N}(0, 1)$. Thus L is now the noise level relative to $\|f\|_{\infty}$. Table 5 presents similar results to that of Table 3 but including the Fourier method $FFTRiesz$, see Eq. (1), for comparison. $FFTRiesz$ is computed with a zero-padding factor of 2 in order to prevent errors due to periodization. We observe that BPD and $iRadonH$ are more robust against noise compared to $FFTRiesz$. This is probably due to the smoothing properties of the Radon transform (integral on lines) and of the back projection (integral operation according to θ).

6. Conclusion

In this work we have introduced a new method, *local in the Radon space*, for the computation of the Riesz transform from the knowledge of the Radon transform. Contrary to previous approaches which involve non-local operators, the proposed algorithm, in even dimension, uses a local derivative of the Radon transform of the data, followed by a vectorial weighted backprojection. Our method is then suitable for computing pointwise the Riesz transform of a function, even if only truncated Radon data are available. Focussing on bidimensional images, we established a very simple Radon based Riesz local formula, which we applied in the context of local tomography: numerical tests conducted on test images, show the interest of the method, in particular to compute the Riesz transform in a Region of Interest (ROI) from associated Radon projections. In such a ROI, the local orientations of the image can also be precisely computed. Finally, we

showed that the proposed approach is more robust to noise (on the image or on its Radon transform) than standard methods.

Acknowledgements

This work was supported by French state funds managed by the ANR within the Investissements d'Avenir program: LabEx CAMI (ANR-11-LABX-0004) and LabEx PERSYVAL-Lab (ANR-11-LABX-0025-01), and within the project ASTRES (ANR-13-BS03-0002-01).

References

- [1] S. Basu, Y. Bresler, $O(N^2 \log_2(N))$ filtered backprojection reconstruction algorithm for tomography, *IEEE Trans. Image Process.* 9 (2000) 1760–1772.
- [2] R. Clackdoyle, M. Defrise, Tomographic reconstruction in the 21st century, *IEEE Signal Process. Mag.* 27 (4) (2010) 60–80.
- [3] R. Clackdoyle, L. Desbat, Data consistency conditions for truncated Fanbeam and parallel projections, *Med. Phys.* 42 (2015) 831–844, <http://dx.doi.org/10.1118/1.4905161>.
- [4] M. Clausel, T. Oberlin, V. Perrier. The monogenic synchrosqueezed wavelet transform: a tool for the decomposition/demodulation of am-fm images. *Appl. Comput. Harmon. Anal.*, 2014, in press <http://dx.doi.org/10.1016/j.acha.2014.10.003>.
- [5] M. Defrise, F. Noo, R. Clackdoyle, H. Kudo, Truncated hilbert transform and image reconstruction from limited tomographic data, *Inverse Probl.* 22 (3) (2006) 1037–1053.
- [6] L. Desbat, R. Clackdoyle, L. Grezes-Besset, C. Mennessier, Cone-Beam imaging of delta functions, in: Nuclear Science Symposium Conference Record, 2006, IEEE, San Diego, CA, USA, vol. 5, pp. 2859–2863. <http://dx.doi.org/10.1109/NSSMIC.2006.356473>.
- [7] M. Felsberg. Low-level image processing with the structure multivector (Ph.D. thesis). Christian-Albrechts-Universitat zu Kiel, Germany, 2002.
- [8] M. Felsberg, R. Duits, L. Florack, The monogenic scale space on a rectangular domain and its features, *Int. J. Comput. Vis.* 64 (2/3) (2005) 187–201.
- [9] M. Felsberg, G. Sommer, The monogenic signal, *IEEE Trans. Signal Process.* 49 (12) (2001) 3136–3144.
- [10] K. Langley, S.-J. Anderson, The Riesz transform and simultaneous representations of phase, energy and orientation in spatial vision, *Vis. Res.* 50 (17) (2010) 1748–1765.

- [11] K.G. Larkin. Topics in multi-dimensional signal demodulation (Ph.D. thesis). University of Sydney, 2000.
- [12] F. Natterer, *The Mathematics of Computerized Tomography*, Teubner-Wiley, Stuttgart, 1986.
- [13] F. Noo, R. Clackdoyle, J.D. Pack, A two step Hilbert transform method for 2D image reconstruction, *Phys. Med. Biol.* 49 (17) (2004) 2525–2546.
- [14] F. Noo, M. Defrise, R. Clackdoyle, H. Kudo, Image reconstruction from fan-beam projections on less than a short-scan, *Phys. Med. Biol.* 47 (July) (2002) 2525–2546.
- [15] T. Rodet, et al., Multichannel algorithm for fast 3D reconstruction, *Phys. Med. Biol.* 47 (2002) 2659.
- [16] A. Sedlazeck. Local feature detection by higher order Riesz transforms on images. Diplomarbeit, Christian-Albrechts-Universität zu Kiel, Germany, 2008.
- [17] C.S. Seelamantula, N. Pavillon, C. Depeursinge, M. Unser, Local demodulation of holograms using the Riesz transform with application to microscopy, *J. Opt. Soc. Am. A* 29 (2012) 2118–2129.
- [18] R. Souillard, P. Carré, A discrete approach to monogenic analysis through Radon transform, in: *Applied Geometric Algebras in Computer Science and Engineering (AGACSE 2012)*, La Rochelle, France, 2012.
- [19] R. Souillard, P. Carré, C. Fernandez-Maloigne, Vector extension of monogenic wavelets for geometric representation of color images, *IEEE Trans. Image Process.* 22 (3) (2013) 1070–1083.
- [20] E.M. Stein, G. Weiss, *Introduction to Fourier Analysis on Euclidean Spaces*, Princeton University Press, New York, 1971.
- [21] M. Unser, D. Van de Ville, Multiresolution monogenic signal analysis using the riesz-laplace wavelet transform, *IEEE Trans. Imag. Process.* 18 (11) (2009) 2402–2418.
- [22] N. Wadhwa, M. Rubinstein, F. Durand, W.T. Freeman, Riesz pyramids for fast phase-based video magnification, in: *2014 IEEE International Conference on Computational Photography (ICCP)*, 2014.
- [23] L. Wietzke, L. Sommer, The conformal monogenic signal, *Pattern Recognit., Lect. Notes Comput. Sci.* 5096 (2008) 527–536.